



A fully-nonlinear computational method for wave propagation over topography

Andrew B. Kennedy^{*}, John D. Fenton¹

Department of Mechanical Engineering, Monash University, Clayton, Victoria 3168, Australia

Received 3 September 1996; accepted 19 June 1997

Abstract

By assuming that the velocity potential is locally represented by a polynomial analytically satisfying Laplace's equation, a method is developed to compute the evolution of surface gravity waves over varying topography for one dimension in plan. This local polynomial approximation (LPA) method is fast and simple and has no essential approximations in its treatment of the free surface boundary conditions. Different degrees of approximating polynomial may be used, which makes the method highly flexible. Conservation of energy considerations and comparison with both analytic results and experimental data show that, with the right choice of parameters, almost any desired level of accuracy may be achieved. © 1997 Elsevier Science B.V.

Keywords: Ocean waves; Surface waves; Numerical models; Shoaling; Wave dispersion

1. Introduction

The propagation of surface gravity waves over varying topography is an important problem in coastal engineering. For wave propagation in one dimension in plan, many approximate solutions to the equations of motion have been developed, almost all assuming irrotational flow in an inviscid fluid, but all suffer from limitations. The shallow water equations are well known but cannot describe steady, progressive waves of finite amplitude, and are unsuitable for many problems of engineering interest. Boussinesq-type equations (Peregrine, 1967; Madsen et al., 1991; Madsen and Sørensen, 1992; Nwogu, 1993; Wei et al., 1995) can model waves which are both steady and

^{*} Corresponding author. Present address: Center for Applied Coastal Research, University of Delaware, Newark, Delaware, USA 19716. E-Mail: kennedy@coastal.udel.edu

¹ Present address: Department of Civil and Environmental Engineering, The University of Melbourne, Parville, Victoria, Australia 3052.

progressive, and extend the practical computational range, but are only mildly nonlinear and lose accuracy as both wave height and water depth increase. The KdV equation (Korteweg and de Vries, 1895; Johnson, 1973) suffers similar problems in addition to being confined to unidirectional waves. Boundary integral equation methods pioneered by Longuet-Higgins and Cokelet (1976) can provide excellent accuracy for any wave height in any water depth and may even be used to describe overturning waves, but these methods have traditionally been extremely expensive computationally. Recently, Wang et al. (1995) used a multi-subdomain approach to reduce the set of matrix equations into a block-banded form, which greatly improved efficiency, but large computers were still needed. Fourier solutions of the full equations of motion can offer good accuracy, but all assume a periodic domain, and most are computationally expensive (Multer, 1973; Fenton and Rienecker, 1982). The Fourier method of Dommermuth and Yue (1987) is quite efficient, but is somewhat difficult to implement for anything other than a level topography. The Green–Naghdi theory of fluid sheets (Green et al., 1974; Webster and Shields, 1991;) also combines accuracy and efficiency, but produces sets of nonlinear equations which very quickly become highly complicated as the level of approximation increases.

In this paper, a method is developed in the time domain for nonbreaking wave propagation in finite depths for one dimension in plan. Potential flow is assumed. The centerpiece of this method is a solution of Laplace's equation using local polynomial approximation (LPA, see Fenton, 1986) of arbitrary order. Due to the use of a local instead of global representation of the velocity potential, the time of solution is directly proportional to the number of computational subdomains. This can provide an excellent combination of accuracy and efficiency, as will be shown.

Emphasis is placed on validating the accuracy of the LPA method using comparisons with analytic results, experimental data, and other computational methods, and through conservation of energy criteria.

2. Governing equations

For irrotational flow of an inviscid, incompressible fluid, all motion may be described by a velocity potential, $\phi(x, y, t)$, such that for two dimensional flow $(u, v) = (\partial\phi/\partial x, \partial\phi/\partial y)$, where (u, v) is the fluid velocity vector, t is time, and x and y are, respectively, the horizontal and vertical coordinates. Throughout the fluid domain, the velocity potential must satisfy Laplace's equation

$$\frac{\partial^2\phi}{\partial x^2} + \frac{\partial^2\phi}{\partial y^2} = 0. \quad (1)$$

At any instant in time, the velocity potential is completely defined by the boundary conditions

$$\phi = \phi_s \text{ on } y = \eta, \quad (2)$$

$$\frac{\partial \phi}{\partial y} - \frac{\partial h}{\partial x} \frac{\partial \phi}{\partial x} = 0 \text{ on } y = h, \tag{3}$$

$$\frac{\partial \phi}{\partial x} = f(x, y, t) \text{ on the left and right boundaries,} \tag{4}$$

where $\phi_s(x, t) = \phi(x, y = \eta, t)$ is the free surface velocity potential, $\eta(x, t)$ is the free surface elevation, and $h(x)$ is the bed elevation. The specification of the function $f(x, y, t)$ will be discussed later, and will vary depending on the type of boundary.

The change of the system in time is governed by the free surface evolution equations. The kinematic free surface boundary condition is

$$\frac{\partial \eta}{\partial t} = \frac{\partial \phi}{\partial y} - \frac{\partial \eta}{\partial x} \frac{\partial \phi}{\partial x} \text{ on } y = \eta. \tag{5}$$

The dynamic free surface boundary condition is based on the unsteady form of Bernoulli’s equation, which may be written as

$$\frac{\partial \phi}{\partial t} = C - gy - \frac{1}{2} \left(\left(\frac{\partial \phi}{\partial x} \right)^2 + \left(\frac{\partial \phi}{\partial y} \right)^2 \right) - \frac{p}{\rho}, \tag{6}$$

where g is gravitational acceleration, p is pressure, which in the absence of surface tension will be taken to be zero at the free surface, and ρ is the fluid density. $C(t)$ is an arbitrary function which is constant through space, but may vary in time. The rate of change of the free surface velocity potential, ϕ_s , may then be calculated as

$$\frac{\partial \phi_s}{\partial t} = \frac{\partial \phi}{\partial t} + \frac{\partial \phi}{\partial y} \frac{\partial \eta}{\partial t} \text{ on } y = \eta. \tag{7}$$

3. Problem definition

Consider the situation shown in Fig. 1. Nonbreaking waves propagate in one dimension in plan over varying topography with no discontinuities in bottom elevation. At time t_0 , both the elevation and velocity potential are known along the free surface. Conditions at the left and right global boundaries are known. Eqs. (5) and (7) may then be used to advance the free surface in time, provided that $\partial \phi / \partial x$, $\partial \phi / \partial y$, and $\partial \eta / \partial x$

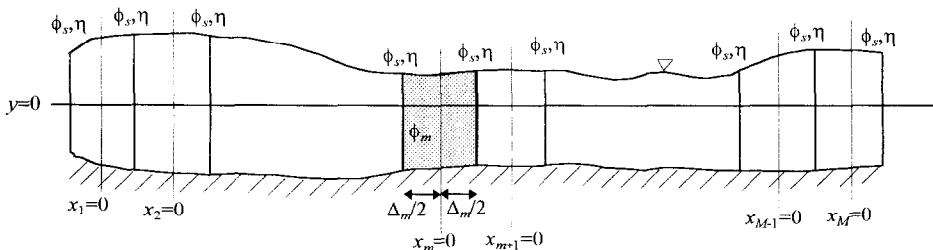


Fig. 1. Definition sketch for wave motion.

are known. $\partial\eta/\partial x$ may be readily estimated using any of a number of standard techniques for numerical differentiation, but to find $\partial\phi/\partial x$ and $\partial\phi/\partial y$ requires the solution of Laplace's equation in two dimensions, a potentially arduous task. However, in finite water depths, it is possible to make assumptions about the structure of the flow which allow for an accurate and highly efficient solution.

4. Solution of Laplace's equation

Consider the velocity potential satisfying Eq. (1)

$$\phi_m(x_m, y, t) = \left[A_{0R} + \operatorname{Re} \left(\sum_{j=1}^{n-1} (A_{jR} + iA_{jI})(x_m + iy)^j \right) + (x_m + iy)^n \begin{cases} A_{nR}, & n \text{ odd} \\ iA_{nI}, & n \text{ even} \end{cases} \right]_m \quad (8)$$

where Re indicates the real part of a complex expression, $i = \sqrt{-1}$, n is an arbitrary integer greater than or equal to three, and the A_j coefficients are independent and may vary in time. This function is defined only in region m , with coordinates (x_m, y) as shown in Fig. 1. Note that x_m is local while y is a global coordinate. If an n value of 3 is substituted into Eq. (8), the velocity potential will contain y^2 terms, as do the Boussinesq equations. It would seem reasonable that larger values of n could give a better approximation and enable the description of more complex flows.

The velocity potential function Eq. (8) may be thought of as having $2n$ independent basis functions which are linearly combined to form ϕ_m . For example, the functions associated with A_{0R} , A_{1R} , and A_{1I} are, respectively, 1, x , and $-y$. The form of these functions is not unique, and linear combinations of them may be made to form new sets of basis functions for ϕ_m . The form of Eq. (8) is the most basic expression of the velocity potential and will be useful when deriving linear dispersion characteristics, but for computational purposes, a different set of basis functions is more efficient. The velocity potential, while still completely equivalent to Eq. (8), will now have the form

$$\phi_m(x_m, y, t) = \left[\sum_{j=0}^{n-1} (B_{jL} \phi_{jL}(x_m, y) + B_{jR} \phi_{jR}(x_m, y)) \right]_m \quad (9)$$

where $[B_{jL}(t)]_m$ and $[B_{jR}(t)]_m$ are the new coefficients in subdomain m , and ϕ_{jL} and ϕ_{jR} are the new basis functions. These new functions ϕ_{jL} and ϕ_{jR} are formed from linear combinations of the old basis functions such that

$$[\phi_{jL}(x_m, y)]_m = \left[Z_{0R} + \operatorname{Re} \left(\sum_{q=1}^{n-1} (Z_{qR} + iZ_{qI})(x_m + iy)^q \right) + (x_m + iy)^n \begin{cases} Z_{nR}, & n \text{ odd} \\ iZ_{nI}, & n \text{ even} \end{cases} \right]_{m,jL} \quad (10)$$

with a similar function for ϕ_{jR} . The coefficients Z_{qR} , etc., are completely specified by satisfying the conditions

$$\phi_{jL} = \begin{cases} y^j, & x_m = -\Delta_m/2 \\ 0, & x_m = \Delta_m/2 \end{cases} \quad \phi_{jR} = \begin{cases} 0, & x_m = -\Delta_m/2 \\ y^j, & x_m = \Delta_m/2 \end{cases} \quad (11)$$

where Δ_m is the width of subdomain m as shown in Fig. 1.

To find these Z coefficients, expand Eq. (8) using the binomial theorem and collect like powers of y to get

$$\begin{aligned} & [\phi_{jL}(x_m, y)]_m = \\ & \left[y^0 i^0 \sum_{q=0}^{nR} \binom{q}{0} Z_{qR} x_m^{q-0} + y^1 i^{1+1} \sum_{q=1}^{nI} \binom{q}{1} Z_{qI} x_m^{q-1} \right. \\ & + y^2 i^2 \sum_{q=2}^{nR} \binom{q}{2} Z_{qR} x_m^{q-2} + y^3 i^{3+1} \sum_{q=3}^{nI} \binom{q}{3} Z_{qI} x_m^{q-3} + \dots \\ & \left. + y^{n-1} \begin{cases} i^{n-1} \sum_{q=n-1}^{nR} \binom{q}{n-1} Z_{qR} x_m^{q-(n-1)}, & n \text{ odd} \\ i^{(n-1)+1} \sum_{q=n-1}^{nI} \binom{q}{n-1} Z_{qI} x_m^{q-(n-1)}, & n \text{ even} \end{cases} \right]_{m,jL} \quad (12) \end{aligned}$$

with a similar expression for ϕ_{jR} where $\binom{a}{b}$ is the binomial function $a!/(b!(a-b)!)$. If n is even, $n_R = n - 1$ and $n_I = n$, and if n is odd, $n_R = n$ and $n_I = n - 1$. For constant x_m , the velocity potential is now seen to be a simple polynomial in y of degree $n - 1$, with the magnitude of each term dependent on the Z coefficients. If ϕ_m is represented in this manner at $x_m = \pm \Delta_m/2$, the coefficients may be found in a straightforward manner by creating a matrix equation in Z_{jR} and Z_{jI} based on Eq. (11) with a different right side for each ϕ_{jL} and ϕ_{jR} .

Next, consider the interior boundary between areas m and $m + 1$, as shown in Fig. 1. Just left of the boundary, at $x_m = \Delta_m/2$,

$$\phi_- = \phi_m(x_m = \Delta_m/2, y, t) = \left(\sum_{j=0}^{n-1} B_{jR}(t) \phi_{jR}(x_m = \Delta_m/2, y) \right)_m$$

while just right of the boundary at $x_{m+1} = -\Delta_{m+1}/2$,

$$\begin{aligned} \phi_+ &= \phi_{m+1}(x_{m+1} \\ &= -\Delta_{m+1}/2, y, t) \\ &= \left(\sum_{j=0}^{n-1} B_{jL}(t) \phi_{jL}(x_{m+1} = -\Delta_{m+1}/2, y) \right)_{m+1} \end{aligned}$$

If $\phi_+ = \phi_-$, it is obvious from Eq. (11) that $(B_{jR}(t))_m = (B_{jL}(t))_{m+1}$. These n continuity arguments may be implicitly implemented by using

$$B_{j,m}(t) = (B_{jR}(t))_m = (B_{jL}(t))_{m+1} \quad (13)$$

as a new coefficient. The velocity potential will now be continuous across the boundary to the zeroth order, the number of independent coefficients is almost halved, and the usefulness of the form of Eq. (9) is justified.

Now that the form of the velocity potential has been established, it is necessary to find coefficients such that the boundary conditions Eqs. (2)–(4) are satisfied as best possible, with the additional constraint that $(\partial\phi/\partial x)_- = (\partial\phi/\partial x)_+$ on interior boundaries.

There are many ways this could be done. Weighted residual techniques spring readily to mind, and since Laplace's equation is analytically satisfied throughout the fluid domain, residuals would only have to be evaluated on the boundaries of the computational subdomains. However, a large number of function evaluations, multiplications, and nested loops would still be required and, instead, a faster collocation method is used.

With the new basis functions Eq. (11) and coefficients Eq. (13), $(M + 1)n$ independent coefficients are needed to globally specify the velocity potential, where M is the number of subdomains. If the velocity potential is equivalently considered to have n degrees of freedom at each interior boundary, and at each of the left and right global boundaries, this method may be easily explained.

Consider, for example, the interior boundary between subdomains m and $m + 1$ as shown in Fig. 1. On the boundary, one constraint sets the velocity potential at the free surface to the known $\phi_s(x)$ Eq. (2) while another imposes the bottom boundary condition Eq. (3) at the bed. The remaining constraints set $(\partial\phi/\partial x)_- = (\partial\phi/\partial x)_+$ at $n - 2$ discrete points on the boundary. At each of the left and right global boundaries, the free surface and the bed are treated in a similar manner, but, to satisfy Eq. (4), $\partial\phi/\partial x$ is set to the known $f(x, y, t)$ at $n - 2$ discrete points, which completes the specification of the velocity potential.

The resulting system of linear equations may be solved at each time step using a banded or block-banded matrix solver. As previously stated, this provides the 'order M ' solution at each time step which is a major advantage of LPA.

All that is left is to determine the locations of the collocation points. Although there are many sets of points which will provide good performance, there is one family of points which also gives the solution some highly desirable qualities. Gauss–Legendre quadrature (e.g., Hornbeck, 1975, p. 154) of level N is a procedure by which the integral of a function over a finite interval may be estimated by knowing the value of the function at the N characteristic Gauss–Legendre points. A polynomial of degree $2N - 1$ or lower will be exactly integrated using this procedure. For example, to estimate the integral of function $g(x)$ over the interval $(-1, 1)$ using Gauss–Legendre quadrature of level $N = 3$, it is necessary to know the value of $g(x)$ at the characteristic Gauss–Legendre points $x = -0.7745966692$, $x = 0$, and $x = 0.7745966692$. These values of $g(x)$ are then multiplied by simple weighing functions to estimate the integral. For integrals over intervals other than $(-1, 1)$, the Gauss–Legendre points are linearly scaled between the limits of integration.

For local polynomial approximation of level n , the velocity difference across interior boundaries $(\partial\phi/\partial x)_- - (\partial\phi/\partial x)_+$ is a polynomial of degree $n - 1$, while $n - 2$ collocation points are available. If this difference were set to zero at the Gauss–Legendre points for $N = n - 2$, taking the free surface and the bed as limits, overall flow between

subdomains would be conserved for $n \geq 4$. For higher values of n , additional weighted moments of flow would also be conserved. This property is considered important enough that in all examples given here, the collocation points are chosen to be the Gauss–Legendre points for $N = n - 2$.

The entire procedure of calculating basis functions and solving Laplace’s equation may, with good coding, be completely automated so that to change the level of LPA approximation (for example, from $n = 5$ to $n = 7$), it would only be necessary to change one entry of an input file. This gives the LPA technique the flexibility to be able to change the level of accuracy easily to suit the requirements of a particular problem.

It should be noted that, instead of matching horizontal velocities across internal boundaries at $n - 2$ collocation points, it is possible to equalize $n - 2$ weighted averages of flow across the boundaries. This removes the problem of choosing the locations of collocation points, and can also be shown to provide good linear dispersion characteristics. However, this idea will not be developed further due to the limitations of space.

5. Linear dispersion characteristics

In the previous section, the computational subdomains were all assumed to be of finite width. However, as mesh lengths go to zero, the continuity conditions between subdomains become a set of differential equations. If the velocity potential is then assumed to have the form of a small amplitude progressive wave, i.e. all coefficients are of the form $\cos(kx - \omega t)$, where k is the wavenumber, and ω is the circular frequency, analytic solutions may be found for the phase speed, c , over a level bed. An outline of this process is given for the simple case of $n = 3$.

Expanding Eq. (8) for the level of approximation $n = 3$, the value of ϕ_m at the right boundary of subdomain m (at $x_m = \Delta_m/2$) is

$$\begin{aligned} &\phi_m(x_m = \Delta_m/2, y, t) \\ &= \left[A_{0R} + A_{1R} \frac{\Delta_m}{2} + A_{2R} \left(\frac{\Delta_m}{2} \right)^2 + A_{3R} \left(\frac{\Delta_m}{2} \right)^3 + y \left(-A_{1I} + A_{2I} \left(-2 \frac{\Delta_m}{2} \right) \right) \right. \\ &\quad \left. + y^2 \left(-A_{2R} + A_{3R} \left(-3 \frac{\Delta_m}{2} \right) \right) \right]_m \end{aligned} \tag{14}$$

Similarly, at the left boundary of subdomain $m + 1$

$$\begin{aligned} &\phi_{m+1}(x_{m+1} = -\Delta_{m+1}/2, y, t) \\ &= \left[A_{0R} + A_{1R} \frac{-\Delta_{m+1}}{2} + A_{2R} \left(\frac{-\Delta_{m+1}}{2} \right)^2 + A_{3R} \left(\frac{-\Delta_{m+1}}{2} \right)^3 \right. \\ &\quad \left. + y \left(-A_{1I} + A_{2I} \left(-2 \frac{-\Delta_{m+1}}{2} \right) \right) + y^2 \left(-A_{2R} + A_{3R} \left(-3 \frac{-\Delta_{m+1}}{2} \right) \right) \right]_{m+1} \end{aligned} \tag{15}$$

For continuity of ϕ across the boundary,

$$\phi_m(x_m = \Delta_m/2, y, t) = \phi_{m+1}(x_{m+1} = -\Delta_{m+1}/2, y, t) \quad (16)$$

This sets up three continuity equations for the constant, y , and y^2 coefficients. The derivation becomes simpler if $[A_{0R}]_{m+1}$, etc. are written as $[A_{0R}]_{m+1} = [A_{0R}]_m + \Delta_m \partial[A_{0R}]_m / \partial x + \dots$, and if it is assumed $\Delta_m = \Delta_{m+1}$. As Δ_m goes to zero, it is then an easy matter to arrive at the differential equations

$$A_{1R} = \frac{\partial A_{0R}}{\partial x} \quad (17)$$

$$2 A_{2I} = \frac{\partial A_{1I}}{\partial x} \quad (18)$$

$$3 A_{3R} = \frac{\partial A_{2R}}{\partial x} \quad (19)$$

where x is now a global variable.

Using a similar process, the condition which specifies that $(\partial\phi/\partial x)_- = (\partial\phi/\partial x)_+$ at collocation point $y = Y_1$ becomes

$$2 A_{2R} = \frac{\partial A_{1R}}{\partial x} - 2Y_1 \frac{\partial A_{2I}}{\partial x} - 3Y_1^2 \frac{\partial A_{3R}}{\partial x} \quad (20)$$

and the bottom boundary condition Eq. (3), for a flat bed, becomes

$$-A_{1I} - 2yA_{2R} = 0 \quad (21)$$

If the bed is assumed to be at $h(x) = 0$, this simplifies to

$$A_{1I} = 0 \quad (22)$$

For small amplitude wave motion, all coefficients will be of the form $A_{0R} = A_{0R}^* \cos(kx - \omega t)$, and the form of the velocity potential will be

$$\phi(x, y, t) = (A_{0R}^* - A_{1I}^* y - A_{2R}^* y^2) \cos(kx - \omega t). \quad (23)$$

Eqs. (17)–(19) may now be used to remove A_{1R} , A_{2I} , and A_{3R} from Eq. (20). Eq. (22) may then be used to further eliminate A_{1I} , and A_{0R} may then be written in terms of A_{2R} . The LPA velocity potential in the small mesh length limit for the level of approximation $n = 3$ then becomes

$$\phi(x, y, t) = A_{2R}^* \left(\frac{-2 + k^2 Y_1^2}{k^2} - y^2 \right) \cos(kx - \omega t) \quad (24)$$

If the kinematic and dynamic free surface evolution Eqs. (5) and (7) are linearized and combined to get

$$\frac{\partial^2 \phi}{\partial t^2} + g \frac{\partial \phi}{\partial y} = 0 \text{ on } y = d, \quad (25)$$

where d is the depth and $y = d$ is thus the still water level, the small amplitude wave speed, $c = \omega/k$, of Eq. (24) is easily shown to be

$$\frac{c^2}{gd} = \frac{1}{1 + ((kd)^2/2)(1 - \alpha_1^2)} \tag{26}$$

where $\alpha_1 = Y_1/d$.

For $n = 4$, a similar process results in

$$\begin{aligned} \frac{c^2}{gd} = & \left[1 + ((kd)^2/12)(2\alpha_1\alpha_2 + 3(\alpha_1 + \alpha_2) - 2(\alpha_1 + \alpha_2)^2) \right] \\ & / [1 + ((kd)^2/6)(3 - (\alpha_1 + \alpha_2)^2 + 4\alpha_1\alpha_2) + ((kd)^4/12) \\ & \times ((\alpha_1\alpha_2)^2 - (\alpha_1 + \alpha_2)^2 + \alpha_1\alpha_2 + (\alpha_1 + \alpha_2))] \end{aligned} \tag{27}$$

For higher levels of approximation, dispersion relationships become quite messy, and explicit formulae will not be given.

Eqs. (26) and (27) are the local polynomial approximation to the exact relationship for small amplitude phase speed

$$\frac{c_{\text{exact}}^2}{gd} = \frac{\tanh(kd)}{kd}$$

It is helpful to compare LPA and exact phase speeds to get a better understanding of the accuracy of LPA. Fig. 2 plots small amplitude phase speed against dimensionless wave number for LPA. Fig. 2 plots small amplitude phase speed against dimensionless wave number for levels of approximation, n , equal to 3, 4, 5, and 7, which have, respectively, 1, 2, 3, and 5 collocation points. Results are given for Y_i (and therefore α_i) values set so that collocation points are at the appropriate Gauss–Legendre points, using the free surface and the bed as limits, and show a clear improvement as the level of approximation, n , increases. Phase speeds for $n = 3$ are reasonable for waves with a dimensionless

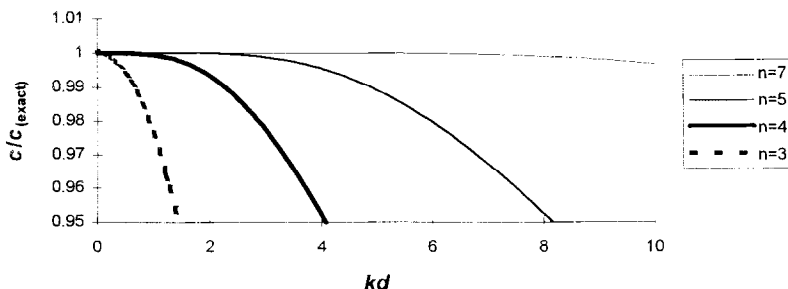


Fig. 2. Local polynomial approximation to small amplitude phase speed.

wavenumber less than $kd = 1.4$ ($\lambda/d \approx 4.5$, where λ is the wavelength), and after this, accuracy deteriorates quickly. Using $n = 4$ gives acceptable agreement up to the nominal deep water limit of $kd = \pi$ ($\lambda/d = 2$). This level of approximation gives a dispersion relationship which is comparable in accuracy to (but different from) the Boussinesq results of Madsen et al. (1991) and Nwogu (1993). Increasing the level of approximation to $n = 5$ gives excellent results even at a depth of $kd = 2\pi$ ($\lambda/d = 1$). With n set to 7, extremely accurate results are found for phase speed in depths up to $kd = 3\pi$ ($\lambda/d = 2/3$), which is indeed a good result for a finite depth method.

It is possible to ‘tune’ phase speeds to more closely approximate the exact small amplitude solution through the adjustment of collocation points, but this is not recommended. If the structure of the velocity potential is inherently inadequate to describe waves of a certain wavenumber, such ‘tuning’ may adversely affect other properties, such as the calculation of bottom velocities, and performance over variable topography. The Gauss–Legendre points provide excellent continuity properties, and phase speeds are seen to improve rapidly with increasing level of approximation, n . Since, as it will be shown, the real power of LPA is with the higher levels of approximation, phase speeds should be good for any reasonable depth.

6. Time stepping

Once the velocity potential function has been determined, the solution may be advanced to the next time step by applying the free surface boundary conditions (Eqs. (5) and (7)) at each computational point. Knowing $\partial\eta/\partial t$ and $\partial\phi_s/\partial t$, the free surface elevations and velocity potentials may be updated using any desired technique. For most calculations presented here, a fourth-order Adams–Bashforth method (AB4, e.g. Hornbeck, 1975, p. 196) was used, since it provided good accuracy while requiring no intermediate steps, which would have been extremely costly. However, computations of wave propagation over a submerged shelf used a third-order Adams–Bashforth method (AB3) for its greater stability. For small amplitude waves travelling over a level bed with no underlying steady current, Von Neumann stability analyses of the AB3 and AB4 methods give the criteria

$$c_{2\Delta_m} \Delta t \leq 0.2303 \Delta_m, \quad (\text{AB3}) \quad (28)$$

$$c_{2\Delta_m} \Delta t \leq 0.1369 \Delta_m, \quad (\text{AB4})$$

where $c_{2\Delta_m}$ is the small amplitude celerity of the smallest resolvable wavelength (with length $\lambda = 2\Delta_m$). These are essentially Courant criteria for the smallest resolvable wavelength, which is linearly the most unstable. Nonlinear stability will, of course, be somewhat different, but Eq. (28) may still serve as a first guide to choosing the time step.

As the AB3 and AB4 methods are not self starting, a fourth-order Runge–Kutta method was used for the first three time steps.

7. Energy integrals

For an inviscid fluid with no external forcing, the sum of potential and kinetic energies should remain constant through time. We therefore use the constancy of this sum as a check on the accuracy of the computations. The potential energy V may easily be shown to be

$$V = \frac{\rho}{2} \int_S (\eta - h_s)^2 dx \quad (29)$$

where S indicates integration over the free surface length, and h_s is the still water datum. For a domain enclosed on all sides but the free surface, and satisfying Laplace's equation, the kinetic energy, T , using the method of Fenton and Rienecker (1982), is

$$T = \frac{\rho}{2} \int_S \phi_s \frac{\partial \eta}{\partial t} dx \quad (30)$$

Both integrals were evaluated by fitting discrete values of the integrand to the same spline used to model the variation in the free surface and bed. The spline was then integrated analytically.

8. Approximation of velocity potential for a regular wave

As a first test of accuracy, LPA solutions of Laplace's equation were used to try to reproduce the kinematics of a regular wave. Test waves were generated with zero Eulerian current using numerical Fourier theory (Rienecker and Fenton, 1981; Fenton, 1988), which gives an accurate waveform and, importantly for the present comparison, provides an exact solution of Laplace's equation throughout the domain.

The resulting free surface elevations and velocity potentials were used as input into the LPA model with periodic global boundary conditions, and a 'goodness of fit' parameter was generated for each wave tested. At the boundaries between computational subdomains, LPA velocities u_s , v_s , and u_b were found, where subscripts s and b here represent, respectively, the free surface and the bed, and horizontal velocities were averaged across the boundary. The exact velocities at these points were then subtracted to give Δu_s , Δv_s , and Δu_b . The 'goodness of fit' parameter was then defined as

$$\Delta u_{\text{RMS}} = \frac{\sqrt{1/3M \sum_{m=1}^M ((\Delta u_s)_m^2 + (\Delta v_s)_m^2 + (\Delta u_b)_m^2)}}{u_{s(\text{exact}),\text{max}}}$$

where $u_{s(\text{exact}),\text{max}}$ is the maximum analytic horizontal velocity at any computational point.

Table 1 plots Δu_{RMS} for various wavelengths, λ/d , against height to depth ratio, H/d , for different levels of approximation, n , and numbers of computational subdomains, M .

As expected, accuracy tends to increase with increasing level of approximation, n . The level $n = 3$ appears to be reasonable only for small, long waves; for all others

velocities are reproduced poorly, and improvement with increasing number of subdomains, M , is poor to nonexistent. However, with n equal to 7, accuracy improves dramatically, as would be expected from knowledge of the linear dispersion characteristics. Even for the highest, shortest waves in Table 1(c), error levels appear to be more than acceptable. Errors also show a steady decrease as the number of subdomains per wavelength increases. The level of approximation $n = 11$ is extremely accurate for every

Table 1
LPA fit to a steady wave

H/d	n	Δu_{RMS}		
		$M = 15$	$M = 30$	$M = 60$
(a) $\lambda/d = 20$				
0.1	3	4.4×10^{-3}	1.1×10^{-3}	1.4×10^{-3}
	7	8.8×10^{-5}	1.9×10^{-6}	2.3×10^{-7}
	11	1.5×10^{-5}	6.4×10^{-9}	5.0×10^{-11}
0.3	3	1.4×10^{-2}	4.8×10^{-3}	4.7×10^{-3}
	7	1.1×10^{-3}	3.3×10^{-5}	3.9×10^{-6}
	11	1.0×10^{-4}	4.1×10^{-6}	5.0×10^{-9}
0.5	3	2.3×10^{-2}	9.5×10^{-3}	8.5×10^{-3}
	7	1.2×10^{-3}	1.3×10^{-4}	1.5×10^{-5}
	11	1.2×10^{-3}	1.1×10^{-5}	1.7×10^{-7}
0.7	3	2.7×10^{-2}	2.0×10^{-2}	1.3×10^{-2}
	7	7.9×10^{-3}	4.1×10^{-3}	4.2×10^{-4}
	11	1.1×10^{-2}	3.0×10^{-3}	7.6×10^{-5}
(b) $\lambda/d = 5$				
0.1	3	2.3×10^{-2}	2.4×10^{-2}	2.5×10^{-2}
	7	2.0×10^{-5}	3.8×10^{-6}	9.1×10^{-7}
	11	2.0×10^{-8}	1.2×10^{-9}	1.9×10^{-10}
0.3	3	2.6×10^{-2}	2.6×10^{-2}	2.6×10^{-2}
	7	6.3×10^{-5}	1.2×10^{-5}	2.9×10^{-6}
	11	9.0×10^{-7}	1.1×10^{-8}	1.5×10^{-9}
0.45	3	3.1×10^{-2}	2.9×10^{-2}	2.9×10^{-2}
	7	2.9×10^{-4}	5.3×10^{-5}	1.2×10^{-5}
	11	1.7×10^{-5}	1.6×10^{-6}	1.9×10^{-7}
(c) $\lambda/d = 2$				
0.05	3	1.3×10^{-1}	1.3×10^{-1}	1.3×10^{-1}
	7	1.8×10^{-4}	4.1×10^{-5}	9.6×10^{-6}
	11	1.0×10^{-7}	2.6×10^{-8}	7.0×10^{-9}
0.1	3	1.2×10^{-1}	1.2×10^{-1}	1.2×10^{-1}
	7	1.7×10^{-4}	4.0×10^{-5}	9.9×10^{-6}
	11	3.3×10^{-7}	6.0×10^{-8}	1.4×10^{-8}
0.15	3	1.1×10^{-1}	1.1×10^{-1}	1.1×10^{-1}
	7	2.0×10^{-4}	4.5×10^{-5}	1.5×10^{-5}
	11	2.4×10^{-6}	3.4×10^{-7}	7.6×10^{-8}
0.2	3	1.0×10^{-1}	1.0×10^{-1}	1.0×10^{-1}
	7	3.7×10^{-4}	8.5×10^{-5}	5.2×10^{-5}
	11	2.1×10^{-5}	2.7×10^{-6}	5.7×10^{-7}

wave tested in Table 1. Its worst performance is with the highest wave in Table 1(a) but, even here, *RMS* errors are less than one part in ten thousand. Since accuracy improves rapidly with increasing number of subdomains, M , this is probably only a problem of resolution. In fact, the accuracy of the level of approximation $n = 11$ is so great that it is not immediately clear that the additional accuracy is even necessary, since the expense of solution will increase significantly over $n = 7$. However, as will be shown later, there are problems sufficiently complex, and with sufficient nonlinearity that the use of such highly accurate approximations may be justified.

The use of n values greater than 11 may require special matrix techniques or a further revision of basis functions, as the large exponents make the matrix equations somewhat ill-conditioned. Using $n = 11$, the potential accuracy of LPA could, in some cases, exceed the accuracy of the matrix solution in double precision.

9. Propagation of a solitary wave

For a first test of the entire procedure, solitary waves were propagated across a level bottom, with height to depth ratios H/d_s ranging from 0.1029 to 0.5346. The waves used were actually pseudo-solitary, consisting of a numerically exact regular wave with length to depth ratio $L/d = 25$ superimposed upon a steady current which opposed any return flow under the trough. The wave was cut at the trough and one wavelength was placed into the computational domain, with smoothing initially provided at the edges. Waves were propagated for distance $25d$ in an enclosed system of length $50d$. For this, and all subsequent computations, the global boundary condition (Eq. (4)) was taken to be a solid vertical wall: *i.e.* $\partial\phi/\partial x = 0$ on the left and right global boundaries.

Fig. 3 shows an example of water surface profiles as the wave propagated from left to right, and also serves as a definition sketch. Note the difference between d and d_s , the still water depths for the original periodic wave and the pseudo-solitary wave, respectively, and h_0 and h_s , the corresponding still water elevations.

To calculate surface and bottom slopes $\partial\eta/\partial x$ and $\partial h/\partial x$, both the free surface and the bed were represented in all computations by one dimensional polynomial splines of degree n , with break points coincident with subdomain boundaries. Since the computational grid remained constant in time, a solution matrix was computed only once, with the consequent savings. For a global boundary condition of a vertical wall, odd spatial derivatives were set to zero at the boundaries.

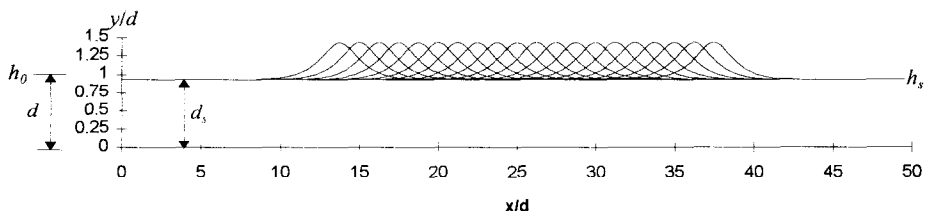


Fig. 3. The propagation of a solitary wave across a level bed.

Energy integrals (Eqs. (29) and (30)) were computed as a general indicator of stability and accuracy. Potential energies were calculated using h_s as datum. A single parameter for global accuracy was given by the relative total energy fluctuations (REF), defined as

$$\text{REF} = \frac{(T + V)_{\max} - (T + V)_{\min}}{(T + V)_{t=0}}$$

Table 2 gives results from the computational runs.

Trends are generally as expected; accuracy increases with increasing number of computational subdomains, M , and number of time steps, K , and with decreasing wave height H/d_s . An increase in accuracy with increasing level of approximation, n , is only weakly apparent and, especially for small waves, fluctuations in energy appear to be mainly controlled by the spatial and temporal resolution. In fact, for the levels of approximation $n = 7$ and $n = 11$, REF values are generally orders of magnitude higher than velocity errors from a wave of similar height in Table 1(a). For such a simple problem, the benefits of a high level of approximation appear to be small.

To some degree, all computations showed growing fluctuations in total energy, although, as is obvious from REF values, these were generally quite small. All computations were stable from the results of the linear stability analysis (Eq. (28)), with the exception of the one asterisked value in Table 2, which was marginally unstable. However, as high frequency oscillations will, in this case, travel with the speed of the solitary wave, which is greater than the small amplitude celerity, the validity of the stability criterion (Eq. (28)) may be brought into question for this, and related problems. It seems obvious that, in some cases, linear stability is not sufficient to ensure nonlinear stability. The sawtooth instability of Longuet-Higgins and Cokelet (1976) was not

Table 2

Energy conservation during solitary wave propagation. Asterisked value is linearly unstable

H/d_s	n	M	REF			
			$K = 75$	$K = 150$	$K = 300$	$K = 600$
0.1029	3	30	7.0×10^{-4}	2.0×10^{-4}		
	7	30	6.5×10^{-4} *	9.1×10^{-5}		
	11	60		2.3×10^{-5}	1.0×10^{-6}	
0.2086	3	30	4.5×10^{-3}	2.2×10^{-3}		
	7	30	7.1×10^{-3}	7.6×10^{-3}		
	11	60		2.1×10^{-4}	7.1×10^{-6}	
0.3161	3	30	1.4×10^{-2}	1.1×10^{-2}		
	7	60		8.6×10^{-4}	7.7×10^{-5}	
	11	60		8.7×10^{-4}	8.8×10^{-5}	
0.4249	3	60		5.4×10^{-3}	4.7×10^{-3}	
	7	60		2.7×10^{-3}	1.1×10^{-3}	
	11	120			1.0×10^{-4}	3.2×10^{-6}
0.5346	3	60		1.2×10^{-2}	1.1×10^{-2}	
	7	120			3.3×10^{-4}	2.0×10^{-5}
	11	120			3.4×10^{-4}	1.1×10^{-5}

observed in any of the cases in Table 2, although it was reproduced if a coarser time step was used.

10. Reflection of a solitary wave by a vertical wall

For a more demanding test, the interaction of two identical, oppositely directed solitary waves or, equivalently, the reflection of a solitary wave by a vertical wall was next modelled. The computational domain consisted of an enclosed system of length $50d$, with initial conditions of two inwardly directed solitary waves. For a given number of time steps, K , used in a computational run, the step size, Δt , was chosen so that the undisturbed solitary wave would have propagated $25d$ in this time. Fig. 4 shows a sequence of water surface profiles which, for clarity of view, end near the center of the interaction.

Several results of engineering interest were obtained from these calculations; namely the maximum water surface elevation at the wall, the maximum force on the wall, and the maximum moment about the base of the wall. These were nondimensionalized as follows:

$$\eta^* = \frac{\eta_{\max} - h_s}{d_s}, \quad F^* = \frac{(\text{force/unit length})_{\max}}{\rho g d_s^2}$$

$$M^* = \frac{(\text{moment about base/unit length})_{\max}}{\rho g d_s^3}$$

Results are summarized in Table 3. It is seen that, to keep errors in total energy small, discretisations in both space and time needed to be much finer than for the case of a propagating solitary wave. This is because the interaction between the two solitary waves was both extremely nonlinear and of short duration. Accordingly, both the accuracy and stability of the time stepping procedure and the ability of the velocity potential to describe the flow field were challenged.

Energy fluctuations (REF) for $n = 3$ were again poor for anything other than the smallest waves. However, it is also of interest that results for the maximum force, overturning moment, and surface elevation appear more robust and seem reasonable for all but the highest waves. The level of approximation $n = 7$ provided good results for all

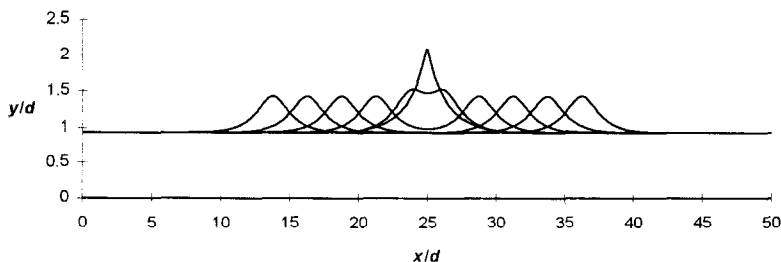


Fig. 4. The collision of two solitary waves of height $H/d_s = 0.5346$, ending near the center of the interaction.

Table 3
The collision of a solitary wave with a vertical wall

H/d	M	K	n	F^*	M^*	A^*	REF
0.1029	120	600	3	0.7167	0.2882	0.2099	3.7×10^{-2}
			7	0.7184	0.2893	0.2117	2.8×10^{-6}
			11	0.7184	0.2893	0.2117	2.9×10^{-7}
0.2086	120	600	3	0.9453	0.4461	0.4305	1.1×10^{-1}
			7	0.9553	0.4536	0.4436	6.1×10^{-5}
			11	0.9553	0.4536	0.4436	1.6×10^{-7}
0.3161	120	600	3	1.1600	0.6259	0.6577	2.0×10^{-1}
			7	1.1828	0.6467	0.7003	4.5×10^{-4}
			11	1.1827	0.6466	0.7003	9.6×10^{-6}
0.4249	200	1000	3	1.3509	0.8081	0.8871	3.2×10^{-1}
			7	1.3848	0.8435	0.9958	5.4×10^{-4}
			11	1.3848	0.8435	0.9957	1.5×10^{-4}
0.5346	400	2500	3	1.5424	0.9841	1.1146	4.6×10^{-1}
	500	3500	7	1.6022	1.0597	1.3686	1.6×10^{-3}
	700	5000	11	1.6022	1.0598	1.3685	8.9×10^{-5}

waves, although, for the highest wave tested, it appeared to be near the limit of its applicability. An n value of 11 provided excellent results for all waves tested.

Computations could become unstable using parameters which would successfully propagate a non-reflecting wave of the same height, although none of these computational runs are included in Table 3. These instabilities ranged from the sawtooth instability of Longuet-Higgins and Cokelet (1976) to total failure. In particular, obtaining an accurate solution for the highest wave tested required many attempts. Fig. 4 shows that, near the center of the interaction, the crest was quite sharp, so a very fine discretisation was needed to resolve it. The growing periodic total energy fluctuations of the previous section were not as important here, since the largest energy variations invariably occurred near the center of the interaction. All of these findings were not

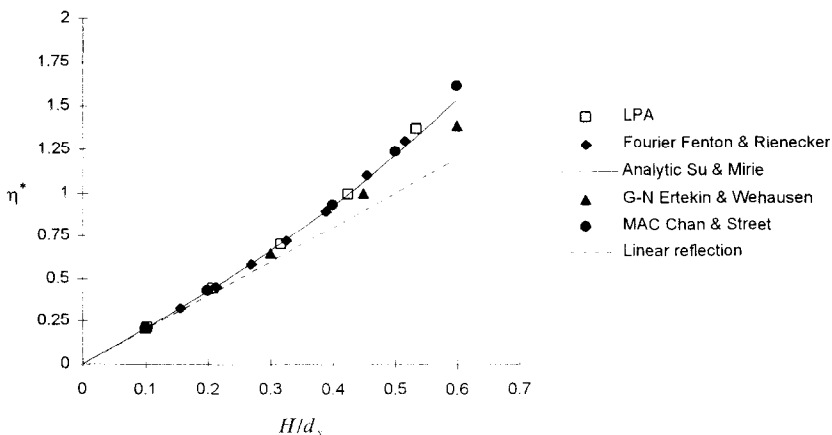


Fig. 5. The maximum runup of a solitary wave on a vertical wall.

entirely unexpected, as this is one of the most demanding problems involving nonbreaking waves.

Some of the results may be compared with similar numerical and analytical studies. Fig. 5 plots the most accurate values of η^* against incident wave height and includes previous analytical and numerical results. All solutions quickly deviate from the assumption of linear reflection for waves greater than $H/d_s = 0.2$, demonstrating the nonlinearity of the problem. The third-order analytical solution of Su and Mirie (1980), and the numerical Green–Naghdi restricted Theory I (G–N) solution of Ertekin and Wehausen (1986) remain good for larger waves but there is some divergence as wave heights continue to increase. Results from the marker and cell (MAC) method of Chan and Street (1970) and the numerical Fourier solutions of Fenton and Rienecker (1982) are highly comparable to present calculations, although there are small differences for the highest waves. Although not shown here, maximum forces and moments from Fenton and Rienecker (1982) also compare well with present results, and it may be consulted for a more detailed qualitative and quantitative analysis of the interaction.

11. Shoaling of a solitary wave

For a final test using solitary waves, the shoaling of a solitary wave of initial height 0.12 was examined. The computational domain had an overall length of $125d$ and consisted of three sections: an initial level of depth d_s and length $25d$, a plane slope of length $10d_s$, and a final shelf with depth d_f . As with the previous two test setups, the boundaries of the computational domain were taken to be vertical walls in order that meaningful conservation of energy values might be obtained. Fig. 6 gives computational details, illustrates the bottom geometry and shows surface profiles of the shoaling waves.

Some features were common to all runs. On the first flat, the wave propagated without change of form. While passing over the slope, the wave height began to increase because of the decreasing depth. Also at this time, as shown in Fig. 6, the front of the wave steepened, and there were small reflections. Once on the final shoal, the wave continued to grow as the advancing mass split into what appeared to be several solitary waves, with the highest at the front.

The behavior of the wave over the final shelf may be quantitatively compared to other results. Analytic solutions to the variable depth KdV equation by Johnson (1973) for solitary waves propagating onto a shoal show fissioning into multiple solitary waves followed by an oscillatory tail, and simple results are found for the number and amplitude of solitary waves developing. For special eigen depths, no oscillatory tail is present. Table 4 compares the most accurate values from the present method to heights analytically predicted for the leading wave by the KdV equation. Results are also included from numerical solutions to Green–Naghdi restricted Theory I (Ertekin and Wehausen, 1986) and a numerical Boussinesq-type solution (Madsen and Mei, 1969). The heights of any trailing solitary waves are not listed as, due to a finite length, they were not always adequately resolved at the end of the computational runs. Results are similar, but show scatter. Green–Naghdi theory consistently underpredicts the height of

the first solitary wave, while, from the one point available, Boussinesq theory gives a result comparable to the LPA solution. The variable depth KdV equation consistently overpredicts wave heights, which is not a great surprise as it does not allow for reflections as the wave progresses up the slope. All methods except LPA are for a relatively low level of approximation, and may become invalid for such highly nonlinear waves as exist on the final shoal.

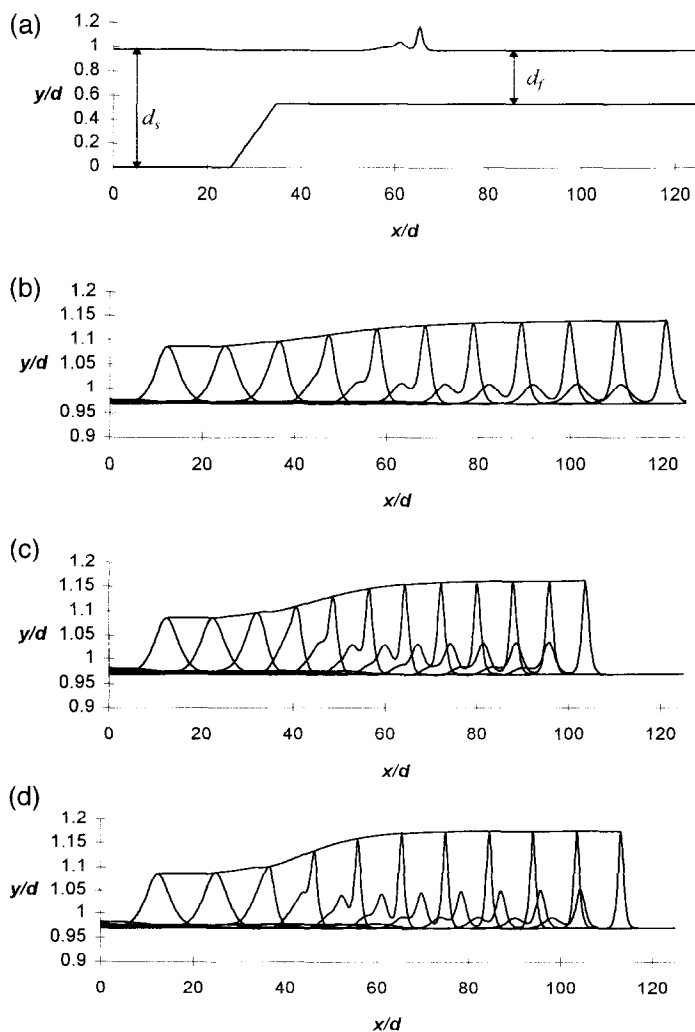


Fig. 6. The propagation of a solitary wave of height $H/d_s = 0.12$ onto a shelf. (a) Bottom topography, (b) $d_t/d_s = 0.6137$, $n = 7$, $M = 300$, $\Delta t(g/d)^{0.5} = 0.06$, $REF = 1.7 \times 10^{-4}$, (c) $d_t/d_s = 0.5$, $n = 7$, $M = 375$, $\Delta t(g/d)^{0.5} = 0.048$, $REF = 3.9 \times 10^{-4}$, (d) $d_t/d_s = 0.4510$, $n = 7$, $M = 600$, $\Delta t(g/d)^{0.5} = 0.03$, $REF = 1.6 \times 10^{-4}$.

Table 4

Heights of leading solitary waves arising from the propagation onto a shelf of a solitary wave of initial height $H/d_s = 0.12$

d_t/d_s	LPA	H/d_s		
		Green–Naghdi	KdV	Boussinesq
0.6137	0.1745	0.168	0.181	
0.5	0.1988	0.184	0.207	0.20
0.4510	0.2120	0.190	0.220	

The first and third shoaling depths shown are KdV eigen depths and, therefore, no trailing oscillatory waves are predicted by that low order theory. For final depth $0.6137d_s$, two solitary waves are predicted to emerge from the wave mass, and for depth $0.4510d_s$, three waves are forecast. LPA solutions clearly showed the emergence of these solitary waves, but solutions for both depths also showed trailing oscillatory waves. However, these were quite small, with amplitudes less than the reflected wave generated as the solitary wave progressed up the slope.

This test setup also required fine discretisations to keep energy fluctuations small. Continually increasing wave heights in shallower depths meant that parameters which might work well at the beginning of the run could cause computations to become unstable as the wave progressed up the slope and across the shelf.

12. Propagation of waves over a submerged shelf

The previous computations involving solitary waves gave a good idea of the potential accuracy of the LPA method, but the behavior of periodic and irregular waves is of much greater engineering interest. This final section computes the propagation of regular waves over a submerged shelf, and results are compared with the experimental and computational results of Ohyama et al. (1995). Fig. 7 shows the experimental setup of the shelf and measurement locations. The wave generator is not shown in the diagram as it was located at a distance $x/d = -56.6$. Although a larger number of experiments were performed, full results were only given for three wave conditions, which were designated cases 2, 4, and 6. These waves had respective periods of $T\sqrt{g/d} = 5.94$, 8.91, and 11.88, and all waves were of initial height $H_0/d = 0.1$. Both experimental and computational runs finished before waves reflecting off the shelf had rereflected off the wave generator and reentered the area of interest. All of the present computations used the level of approximation $n = 7$ along with a spatial discretisation of $\Delta x/d = 0.1$ and a time step of $\Delta t\sqrt{g/d} = 0.0198$.

Waves were generated computationally by specifying a time series of velocity at collocation points on the generating boundary. For stability, the free surface slope at the boundary, $\partial\eta/\partial x$, was specified using the analytic expression for the slope of the target wave, while slopes near the boundary were calculated using second and fourth order

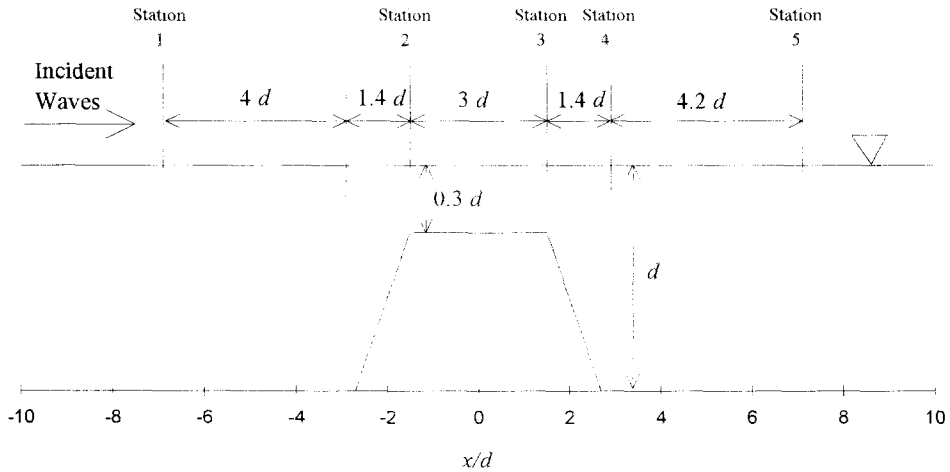


Fig. 7. Experimental setup for wave propagation over a submerged shelf.

central differences. Fully nonlinear time series of velocities and surface slopes were taken from steady waves generated using the method of Fenton (1988).

At the far end of the domain, waves entered a special propagation zone in which the free surface evolution equations Eqs. (5) and (7) gradually changed to become the advection equations

$$\frac{\partial}{\partial t} \left(\frac{\partial \eta}{\partial x} \right) = -c \frac{\partial}{\partial x} \frac{\partial \eta}{\partial x} \quad (31)$$

and

$$\frac{\partial}{\partial t} \left(\frac{\partial \phi_s}{\partial x} \right) = -c \frac{\partial}{\partial x} \frac{\partial \phi_s}{\partial x} \quad (32)$$

where c is the small amplitude phase speed for the periodic wave. These equations were solved in finite difference form using an upwinding scheme. At the exiting boundary, the specified horizontal velocity distribution was calculated from linear theory and the free surface elevation at the boundary. The effect of these conditions was to ensure that any errors arising from an imperfect boundary condition could not propagate back into the area of interest, because they would continuously be advected out of the domain. For simple test cases of regular waves propagating over a level bed, reflection from the exiting boundary was found to be so small as to be negligible.

Figs. 8 and 9 show computed and measured time series at Stations 3 and 5, as defined in Fig. 7. An overall phase shift was applied to the computational results for each wave case so that the phase would match the experimental data. Elevation traces at Station 3 show that the waves have shoaled significantly on the shallow crest, and all time series show tails which have been shed behind the main body of the wave. Wave heights on

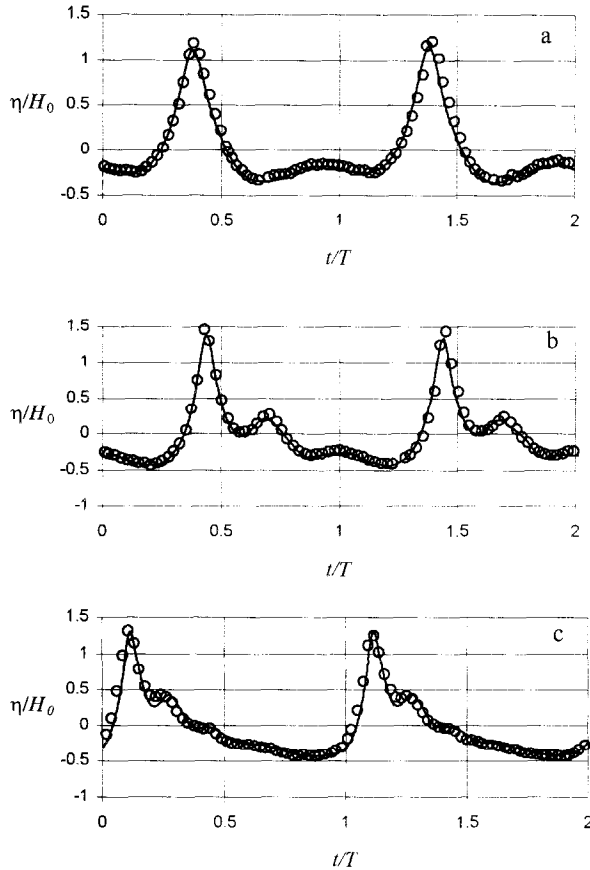


Fig. 8. Computed (lines) and measured (symbols) time traces of surface elevation at station 3. (a) Case 2, (b) case 4, (c) case 6.

the shelf are very large, especially in cases 4 and 6, where the height to depth ratios at Station 3 are around 0.6. Agreement with computations is excellent. The LPA model shows a slight tendency to underpredict crest heights, but this was also a feature of the Boundary Integral Equation Method (BIEM) solutions of Ohyama et al. (1995).

However, although these results at Station 3 are quite good, Ohyama et al. also obtained reasonable results at this station using the Boussinesq model of Nwogu (1993), which has a considerably lesser computational cost than either LPA or BIEM. However, the Boussinesq model proved unable to accurately model the decomposition of the wave after the shelf into higher harmonics, as measured at Station 5. Fig. 9 shows LPA and measured time series at Station 5. For all cases, LPA results agree very well with the experimental data, and can predict both the magnitudes and phases of the multicrested sea state. The present results are actually better overall than the BIEM solutions of Ohyama et al. (1995). Since the potential accuracy of BIEM is greater than that of LPA using $n = 7$, the reason for this is likely that the finer spatial and temporal resolution of

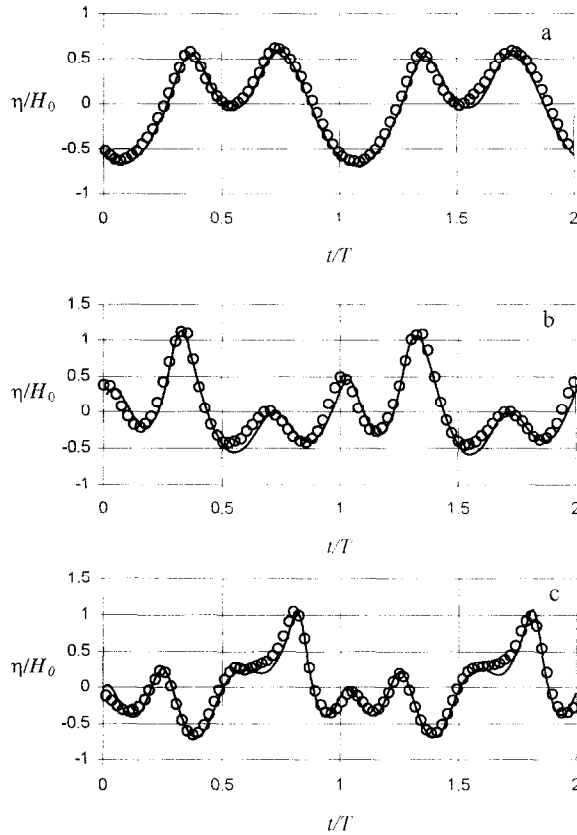


Fig. 9. Computed (lines) and measured (symbols) time traces of surface elevation at station 5. (a) Case 2, (b) case 4, (c) case 6.

the present computations allowed them to better capture the features of the wave motion. This greater resolution was made possible by the significantly lower computational cost of LPA when compared to BIEM.

As a matter of comparison, computations were also performed using the LPA level of approximation $n = 5$ with the same spatial and temporal resolution, but will not be shown here. Results at Station 3 were almost identical to those computed previously using $n = 7$, but results at Station 5 were not as good. Since the linear dispersion relationship for the level of approximation $n = 5$ is good up to a wavenumber of $kd = 2\pi$, which is much shorter than any of the primary wavelengths, this discrepancy is somewhat surprising. However, computation of the nonlinear decomposition of the wave on the downslope and trough is a significantly more demanding task, and necessitates a good representation of the nonlinear interaction of free and forced waves for several higher harmonics. The lower level of approximation assumed using $n = 5$ simply was not able to accurately model the fluid velocities in this situation, and the computational results reflected this.

13. Computational speed

Several times previously it has been mentioned that, because of the local approximation which results in a block banded matrix structure, LPA provides an accurate and efficient solution of Laplace's equation. The accuracy of LPA has been shown using a number of tests, and quantitative results are now given to demonstrate its efficiency. An industry standard measure of floating point processor performance, SPECfp92 (Dixit, 1992), is used to compare CPU cost/time step for LPA and BIEM across different platforms.

On a DEC Alpha 3000 model 300LX with a SPECfp92 of 77.7, a medium sized computation with 250 surface points (249 subdomains) using the level of approximation $n = 7$ takes almost exactly 0.5s CPU/time step. Because of the block banded nature of the LPA matrix equations, run times for computations with a greater or lesser number of subdomains may be linearly scaled from this. For the levels of approximation $n = 3$ and $n = 11$, times may be multiplied by 0.18 and 2.89 respectively.

These times may be compared with BIEM results for the model of Grilli et al. (1989). For a computation with 250 surface points running on a Sparc Station Ultra 1 with a SPECfp92 of 351, computational times range from 18s–23s CPU/time step, depending on the topography. After scaling to a SPECfp92 of 77.7, this becomes 81s–104s CPU/time step. For larger or smaller problems, CPU cost is proportional to (total nodes) ^{r} , where r varies between 2.0 and 3.0 depending whether adaptive integration is necessary. The authors would like to thank Stephan Grilli for providing the above information on BIEM computational costs.

The cost of BIEM using the multi-subdomain method of Wang et al. (1995) may now be estimated. They state that the controlling cost in BIEM is usually the time in generating the coefficient matrix, T_{CM} . From Fig. 3(a) of their paper, the ratio of T_{CM} using the multi-subdomain approach over a flat bed with 10 panels on interior boundaries to T_{CM} using normal BIEM is approximately 0.3. Applying this to the scaled results of Grilli gives a rough estimate of CPU cost/time step of 24s–31s with SPECfp92 = 77.7. Because of the multi-subdomain approach, costs for larger or smaller problems may be linearly scaled.

These results indicate a clear advantage in speed for LPA (0.5s vs. 24s–31s). However, there are some factors which will reduce this difference somewhat. The first is the tendency of computational nodes in BIEM to cluster around areas of high curvature, which effectively increases resolution over a fixed grid approximation with the same number of surface points. The second is that BIEM generally uses larger time steps than LPA. Still, a significant difference in computational speed will remain.

14. Discussion and conclusions

The LPA method developed here has been shown to provide excellent accuracy with a reasonable cost over a wide range of test cases. Analytic results, comparisons of velocity errors with exact solutions, and time domain computations have all demonstrated the effectiveness of the LPA technique.

The use of a polynomial series of arbitrary degree permits great flexibility, as a lower level of approximation may be used for mildly dispersive, mildly nonlinear problems, while highly nonlinear problems such as the collision of large solitary waves may be represented very well using a polynomial of higher degree. Analytic solutions of the LPA linear dispersion relationship can provide a basic guideline for the accuracy of a given level of approximation, although nonlinear considerations are also very important.

The necessary spatial and temporal resolution required to accurately solve a given problem is also important. As the nonlinearity of the problem grows, the resolution needed to solve a problem accurately increases greatly. In this paper, the necessary mesh size was generally found by trial and error, and accuracy was verified by comparison with some independent criterion. Unfortunately, no hard and fast rules were found, although the examples given here can provide a guide for similar problems. However, as LPA has a relatively low computational cost, it takes little additional effort to run a problem more than once with different resolutions to compare results.

As derived here, LPA is only applicable for wave propagation for one dimension in plan. However, a variant using many of the same principles which is valid for three dimensional fluid motion is presented in Kennedy and Fenton (1996). Another variant of the present method uses the mode-coupling expansion of Dommermuth and Yue (1987), along with further revision to velocity potential basis functions, to greatly increase speed, although some accuracy is sacrificed for higher waves. All of these methods are fully detailed in Kennedy (1997).

References

- Chan, R.K., Street, R.L., 1970. A computer study of finite-amplitude water waves. *J. Comp. Phys.* 6, 68–94.
- Dixit, K.M., 1992. New CPU Benchmark Suites from SPEC, Proc. 37th Annual IEEE Int. Comp. Conf. – COMPCON Spring '92, San Francisco, pp. 305–310.
- Dommermuth, D.G., Yue, D.K.P., 1987. A high-order spectral method for the study of nonlinear gravity waves. *J. Fluid Mech.* 184, 267–288.
- Ertekin, R., Wehausen, J., 1986. Some soliton calculations, Proc. 16th Symp. Naval Hydrodyn., Berkeley, pp. 167–184.
- Fenton, J.D., 1986. Polynomial approximation and water waves, Proc. 20th Int. Conf. Coastal Engng, Taipei, pp. 193–207.
- Fenton, J.D., 1988. The numerical solution of steady water wave problems. *Comput. Geosci.* 14, 357–368.
- Fenton, J.D., Rienecker, M.M., 1982. A Fourier method for solving nonlinear water wave problems: Application to solitary wave interactions. *J. Fluid Mech.* 118, 411–443.
- Green, A., Laws, N., Naghdi, P., 1974. On the theory of water waves. *Proc. R. Soc. London A* 338, 43–55.
- Grilli, S.T., Skourup, J., Svendsen, I.A., 1989. An efficient boundary element method for nonlinear water waves. *Eng. Anal. Boundary Elem.* 6, 97–107.
- Hornbeck, R., 1975. *Numerical Methods*, Prentice-Hall Inc., Englewood Cliffs, NJ.
- Johnson, R.S., 1973. On the development of a solitary wave moving over an uneven bottom. *Proc. Camb. Philos. Soc.* 73, 183–203.
- Kennedy, A.B., 1997. The computation of wave propagation over varying topography, PhD thesis, Monash University, in preparation.
- Kennedy, A.B., Fenton, J.D., 1996. A fully nonlinear 3D method for the computation of wave propagation, Proc. 25th Int. Conf. Coastal Eng., Orlando.
- Korteweg, D.J., de Vries, G., 1895. On the change of form of long waves advancing in a rectangular canal, and on a new type of long stationary waves. *Philos. Mag.* 39 (5), 422–443.

- Longuet-Higgins, M.S., Cokelet, E.D., 1976. The deformation of steep surface waves on water, I. A numerical method of computation. *Proc. R. Soc. Lond. A* 350, 1–26.
- Madsen, O., Mei, C., 1969. The transformation of a solitary wave over an uneven bottom. *J. Fluid Mech.* 39, 781–791.
- Madsen, P.A., Murray, R., Sørensen, O.R., 1991. A new form of the Boussinesq equations with improved linear dispersion characteristics. *Coastal Eng.* 15, 371–388.
- Madsen, P.A., Sørensen, O.R., 1992. A new form of the Boussinesq equations with improved linear dispersion characteristics. Part 2 A slowly-varying bathymetry. *Coastal Eng.* 18, 183–204.
- Multer, R., 1973. Exact nonlinear model of wave generator. *J. Hyd. Div. ASCE* 99, 31–42.
- Nwogu, O., 1993. An alternative form of the Boussinesq equations for nearshore wave propagation. *J. Waterway Port Coastal and Ocean Eng.* 119, 618–638.
- Ohyama, T., Kioka, W., Tada, A., 1995. Applicability of numerical models to nonlinear dispersive waves. *Coastal Eng.* 24, 297–313.
- Peregrine, D., 1967. Long waves on a beach. *J. Fluid Mech.* 27 (4), 815–827.
- Rienecker, M.M., Fenton, J.D., 1981. A Fourier approximation method for steady water waves. *J. Fluid Mech.* 104, 119–137.
- Su, C., Mirie, R., 1980. On head-on collisions between two solitary waves. *J. Fluid Mech.* 98, 509–525.
- Wang, P., Yao, Y., Tulin, M., 1995. An efficient numerical tank for nonlinear water waves, based on the multi-subdomain approach with BEM. *Int. J. Numer. Meth. Fluids* 20, 1315–1336.
- Webster, W., Shields, J., 1991. Applications of high-level Green–Naghdi theory to fluid flow problems, *Proc. Symp. Dynamics Marine Vehicles and Structures in Waves*, Elsevier, pp. 109–124.
- Wei, G., Kirby, J., Grilli, S., Subramanya, R., 1995. A fully nonlinear Boussinesq model for surface waves. Part 1 Highly nonlinear unsteady waves. *J. Fluid Mech.* 294, 71–92.